New Journal of Physics
The open access journal at the forefront of physics

Deutsche Physikalische Gesellschaft DPG IOP Institute of Physics

PAPER • OPEN ACCESS

Preparation and characterization of narrow bandgap ferroelectric $(K,Ba)(Ni,Nb)O_{3-\delta}$ films for mesoporous all-oxide solar cells

To cite this article: Chuanqing Li *et al* 2019 *New J. Phys.* **21** 013011

New Journal of Physics
The open access journal at the forefront of physics

Deutsche Physikalische Gesellschaft DPG
IOP Institute of Physics

Published in partnership with: Deutsche Physikalische Gesellschaft and the Institute of Physics

OPEN ACCESS

RECEIVED
12 October 2018

REVISED
5 December 2018

ACCEPTED FOR PUBLICATION
17 December 2018

PUBLISHED
18 January 2019

PAPER

Preparation and characterization of narrow bandgap ferroelectric (K,Ba)(Ni,Nb)$O_{3-\delta}$ films for mesoporous all-oxide solar cells

Chuanqing Li[1,2], **Anyang Cui**[1], **Fangfang Chen**[1], **Kai Jiang**[1], **Liyan Shang**[1], **Jinchun Jiang**[1], **Zhigao Hu**[1,3] and **Junhao Chu**[1,2]

[1] Key Laboratory of Polar Materials and Devices (MOE) and Technical Center for Multifunctional Magneto-Optical Spectroscopy (Shanghai), Department of Electronic Engineering, East China Normal University, Shanghai 200241, People's Republic of China
[2] National Laboratory for Infrared Physics, Shanghai Institute of Technical Physics, Chinese Academy of Science, Shanghai 200083, People's Republic of China
[3] Collaborative Innovation Center of Extreme Optics, Shanxi University, Taiyuan, Shanxi 030006, People's Republic of China

E-mail: zghu@ee.ecnu.edu.cn

Keywords: ferroelectric polarization, hysteretic behavior, bandgap, photovoltaics effects, perovskite solar cells

Supplementary material for this article is available online

Abstract

Ferroelectric (K,Ba)(Ni,Nb)$O_{3-\delta}$ films have triggered intense studies for applications in photovoltaic device due to their efficient ferroelectric polarization-driven carrier separation and above-bandgap generated photovoltages. However, they are suffered from a challenge of preparation limiting novel device architectures. Meanwhile, the bandgap for most of ferroelectric materials reported so far is still too large to be considered for desirable spectral absorption. Here, we propose a unique strategy to successfully synthesize the (K,Ba)(Ni,Nb)$O_{3-\delta}$ films with the lower bandgap of about 1.45 eV. A new cell structure of utilizing (K,Ba)(Ni,Nb)$O_{3-\delta}$ as a active layer is explored to interface with electron-transporting TiO_2. Such mesoporous-ferroelectric combination solar cell is beneficial for facilitating the extraction of photocarriers. Under standard AM 1.5G irradiation, the optimized (K,Ba)(Ni, Nb)$O_{3-\delta}$ film solar cell exhibits a higher open-circuit voltage of 1.27 V than those of previous reports on ferroelectrics. Furthermore, a fill factor of 64% and a power conversion efficiency of 0.2% are achieved via the polarization switching modulation. The present results provide a novel synthetic approach toward developing high performance solar cells based on lead-free ferroelectric films.

1. Introduction

Since the discovery of the ferroelectric photovoltaic (FPV) effect for the $(KNbO_3)_{1-x}(BaNi_{1/2}Nb_{1/2}O_{3-\delta})_x$ (KBNNO*x*) solid solutions, these materials have been increasingly investigated for photovoltaic (PV) and photocatalytic devices [1–3]. Under illumination, ferroelectric (FE) materials exhibit a reversibly switchable photocurrent and the above bandgap open circuit voltages [4–9]. Compared to the PV effect of traditional *p-n* junction devices, [10, 11] for the FPV effect, photon-generated electron–hole (*e*–*h*) pairs are separated without the presence of a gradient for the electrochemical potential [12, 13]. While the FPV effect is derived from the polarization switching-modulated energy band of the heterostructure, which can be also summarized as the polarization-induced build-in field [14]. Recent studies have confirmed that PV parameters of FE-based solar cells, including open-circuit voltage (V_{OC}), short-circuit current (J_{SC}), and power conversion efficiency (PCE) [15] can be dramatically enhanced by tuning FE bandgap (E_g) and switching FE polarization [16–19]. However, the wide E_g of reported FE absorbers exceeds the optimum value of solar spectrum center, which corresponds to the maximum theoretical PCE, [20] and leads to the poor sunlight absorption capabilities. The wide E_g of typical ferroelectric perovskites is ascribed to the metal-oxygen bonds at B sites and the large difference in their electronegativities. Due to the merit of the narrow bandgap of 2.7 eV, $BiFeO_3$ (BFO) has been widely studied for PV applications [9, 21]. Nevertheless, the photovoltaic efficiency has been stillinhibited by the wide bandgap, which only allows the use of 8%–20% of the solar spectrum. Therefore, lowering the E_g value of novel

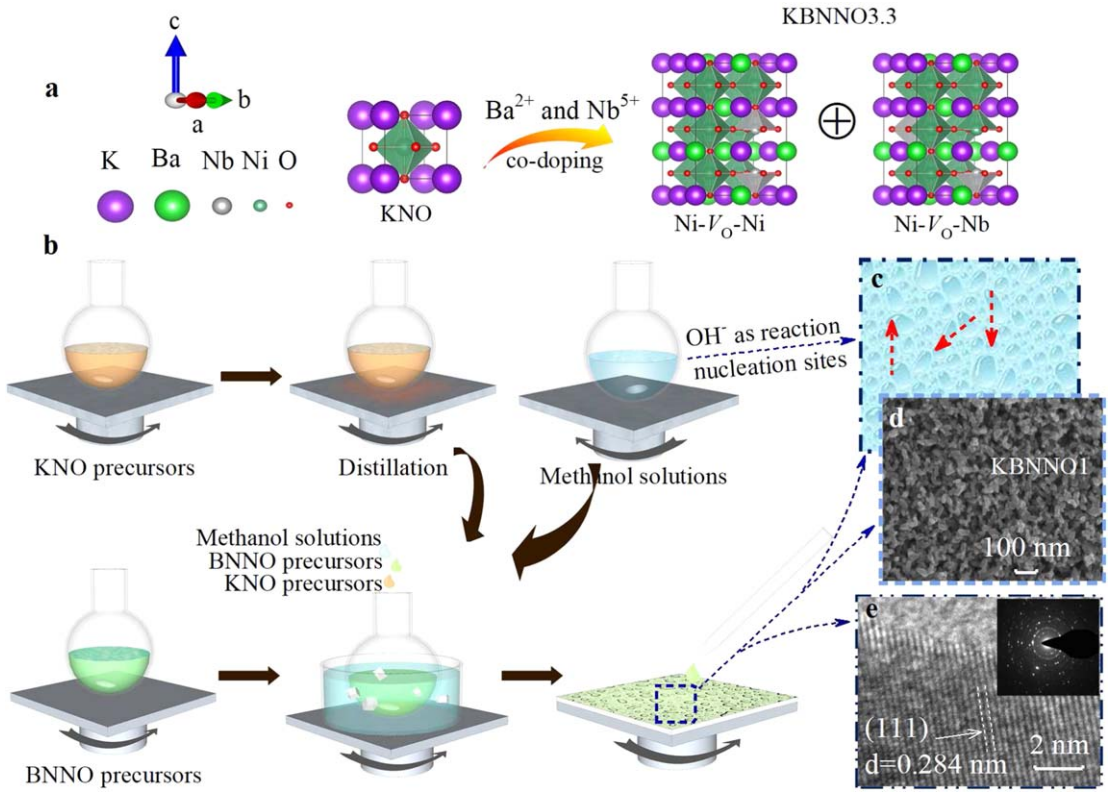

Figure 1. (a) The atomic structure representation of the $KNbO_3$ and KBNNOx ($x = 0.33$). It exhibits two stable KBNNO3.3 configurations with the local structure of Ni^{2+}–V_O–Ni^{2+} and Ni^{2+}–V_O–Nb^{5+}. (b) Schematic diagrams for fabrication process of KBNNOx films. (c) The OH^- ions as reaction nucleation sites. (d) and (e) High resolution TEM image in selected area from KBNNO1 crystalline films, respectively.

materials without affecting the ferroelectric properties is a cost-effective way to obtain PV devices with higher PCE. Fortunately, followed above method, the lower bandgap of 1.39 and 1.4 eV for $(KNbO_3)_{1-x}(BaNi_{1/2}Nb_{1/2}O_{3-\delta})_x$ ($x = 0.1$) solid solutions and Bi_2FeCrO_6 (BFCO) have been demonstrated [1, 22]. Therefore, chemical modified the perovskite B site by transition metal is a promising guide for engineering the value of E_g [23–26]. Nevertheless, the potential of semiconducting FE films in actual solar energy conversion is remained highly expectant.

In this work, we demonstrate a unique route to synthesis light absorbers to develop FE-based solar cells by exploring the properties of KBNNOx films. The present method is based on forming nucleation sites (deionized water as the growth medium) and tailoring Ni^{2+}–V_O–Nb^{5+} and Ni^{2+}–V_O–Ni^{2+} configurations in the film to realize effectively tuning of bandgap and FE properties for KBNNOx. The film crystallizes in two different transition-metal cations of Nb^{5+} and Ni^{2+} on the perovskite B sites, as shown in figure 1(a). It is apparent that ferroelectricity is driven by the Nb^{5+} ions and E_g is controlled by the interaction between Ni^{2+} and Nb^{5+} via V_O. The simultaneous occurrence of the two mechanisms represents the successfully synthesis of the semiconducting KBNNOx films accompanying optimum ferroelectricity-optical absorption combinations for solar cell applications. Furthermore, we used KBNNOx as a film sensitizer to interface with electron-transport material (TiO_2) and hole-transport material (HTM, p-type NiO) to achieve a kind of all-oxide heterojunction cell. Under illumination, the optimal KBNNOx solar cell exhibits a PCE of 0.2% and a fill factor (FF) up to 64% by applying FE polarization, which is firstly reported for KBNNO1 PV devices. The present results provide critical insights into both understanding and optimizing the FEPV properties in KBNNOx.

2. Experimental details

2.1. Synthesis of material

Stoichiometric quantities of potassium acetate [$K(CH_3COO)$, 99%] and niobium ethoxide [$Nb(CH_3CH_2O)_5$, 99.9%] were mixed in ethanol solution without the use of glove box, and then refluxed for 12 h to form the homogeneous $KNbO_3$ (KN) precursor. The precursor was added to a mixture with the mole ratio barium acetate [$Ba(CH_3COO)$, 99%]/Nickel tetrahydrate [$Ni(CH_3COO)_2{\cdot}4H_2O$, 98%]/$Nb(CH_3CH_2O)_5$ = 2/1/1 to obtain 0.3 M KBNNOx solutions. A 3 M deionized aqueous solution was prepared using methanol as solvent. Finally,

the KBNNOx precursors were hydrolyzed by the addition of deionized aqueous solution in a ratio of water/alkoxide = 0.3.

2.2. Ferroelectric perovskite solar cells fabrication

Fluorine-doped SnO_2 (FTO) glass were cleaned sequentially in deionized water, acetone, isopropanol, and ethanol. For the mesoporous-type device, 40 nm compact TiO_2 (c-TiO_2) blocking layer was spin-coated on the FTO substrate at 3000 rpm for 30 s and baked at 450 °C for 1 h. The c-TiO_2 precursor was synthesized with the molar ratio of titanium isopropoxide/HCl = 1.5/0.13. Next, the diluted TiO_2 paste (Dyesol 30NR-D) was deposited on the c-TiO_2 layer and sintered at 550 °C for 1 h, resulting in the formation of mesoporous TiO_2 (m-TiO_2) layer. The KBNNOx precursor was grown on the m-TiO_2 layer for twelve times with 2500 rpm for 30 s. Each coating layer was sintered at 320 °C for 5 min. Then, all the films were baked at 550 °C for 30 min. Similarly, a 60 nm thick NiO layers were prepared and pre-annealing at 280 °C for 5 min. The NiO precursors with 0.1 M concentration was prepared by dissolving nickel (II) acetate tetrahydrate [$Ni(CH_3COO)_2{\cdot}4H_2O$, 98%] and monoethanolamine in ethanol. The samples were annealed at 500 °C for 30 min. Then, 50 nm thick Au electrodes were sputtered on top of the NiO layer with fringe shape, resulting in a cell area of 0.01 cm^2. Note that the planar configuration device without m-TiO_2 layer was deposited on c-TiO_2 layer. The procedures for fabricating the c-TiO_2, KBNNOx, NiO, and Au layers are the same as mesoporous-type device.

2.3. Characterization

Crystallographic structure of the films was characterized by x-ray diffraction (XRD) with Cu Kα radiation (D/MAX-2550 V, Rigaku Co.). Temperature dependent Raman spectra were measured using a micro-Raman spectrometer with a spectral resolution of 0.65 cm^{-1} (Jobin-Yvon LabRAM HR Evolution). A Nd:YAG laser with a wavelength of 532 nm was taken as the exciting source. The absorption spectra were measured by the ultraviolet-visible-near infrared (UV–vis-NIR) spectrophotometer (cary500, USA Varian) equipped with integration sphere. Scanning electron microscopy (SEM) and energy-dispersive x-ray spectroscopy of the devices were performed (FEI Nova Nano). Ultraviolet photoelectron spectroscopy characterizations were investigated by monochromatized HeI radiation at 21.22 eV. The photovoltaic outputs were excited by solar-simulated AM1.5 sunlight (100 mW cm^{-2}, Sol 3A solar simulator, Newport Orial). The current density-voltage characteristics were recorded using Keithley 2400.

3. Results and discussions

3.1. High-quality ferroelectric KBNNOx films

Ferroelectric oxide $(KNbO_3)_{1-x}(BaNi_{1/2}Nb_{1/2}O_{3-\delta})_x$ (KBNNOx, $x = 0.0$, 0.1, 0.2, and 0.3, abbreviated as KNO, KBNNO1, KBNNO2, and KBNNO3) films were fabricated using the chemical solution deposition (CSD) method. Particularly, synthesis of multicomponent crystalline oxides by CSD method is commonly complicated due to the different rates of the hydrolysis for individual component of compounds. The present study has demonstrated that the co-presence of ethoxide and methoxide in precursor could effectively alleviate this problem. Moreover, few works to date have been reported on the influence of hydrolytic process on the development of microstructure in KBNNOx films. Figure 1(a) displays the atomic structures of the KNO and KBNNO3.3 with the aided of the first-principles density functional theory calculations. Note that the theoretical information about the detailed calculation and analysis of the above materials could be found in previous work [1–3, 22]. Figure 1(b) provides the fabrication parameters, such as distillation, deionized water of hydrolysis, and hydrolysis temperature. Furthermore, as shown in figure 1(c), the OH^- ions attached to the substrate in a high-density monolayer might result in the formation of a small number of seeds, which acted as nucleating sites for KBNNOx. As an example, the seeds subsequently grown by progressive incorporation of precursors from the KBNNO1 solution could form three-dimensional nanometre-sized crystals (figure 1(d)). The reasonable chemical states of the as-grown KBNNO1 films were confirmed by x-ray photoemission spectroscopy, which are shown in figure S1 available online at stacks.iop.org/NJP/21/013011/mmedia. Finally, the corresponding high resolution TEM (figure 1(e)) image shows that the d-spacing is about 0.284 nm, which is in accordance with the (111) plane of KBNNO1 films. Note that the perfect lattice fringe suggests the high quality of the present films.

3.2. Design and characterization of KBNNO1 solar cells

To investigate the absorption properties of KBNNOx films, as an example, KBNNO1 planar and mesostructured heterojunctions were constructed (figures 2(a) and (b)), which were abbreviated as NiO/KBNNO1/c-TiO_2/FTO and NiO/KBNNO1/m-TiO_2/c-TiO_2/FTO, respectively. TiO_2 has been recognized as one of the material of possessing the stabilization, environment-friendly characteristics, and high electron mobility for applications in dye-sensitized and perovskite devices. Similar to the dye-sensitized solar energy conversion, the incorporation of

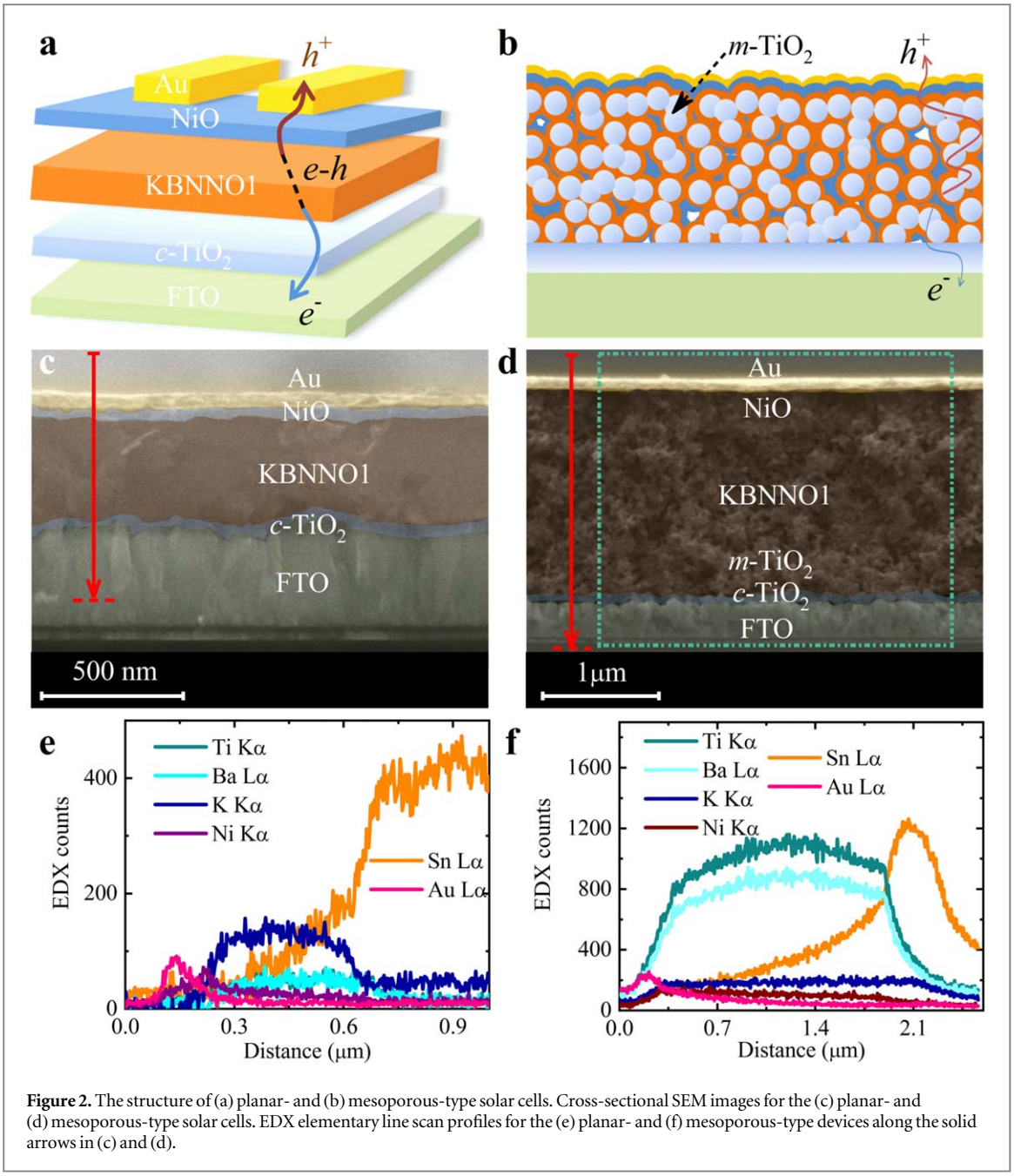

Figure 2. The structure of (a) planar- and (b) mesoporous-type solar cells. Cross-sectional SEM images for the (c) planar- and (d) mesoporous-type solar cells. EDX elementary line scan profiles for the (e) planar- and (f) mesoporous-type devices along the solid arrows in (c) and (d).

mesoporous composites for KBNNO1/c-TiO_2 interface can increase the surface area of absorbing layer, which enables a more effective photon-generated carriers separation and collection [27, 28]. The hole mobility of p-type NiO is 25 $cm^2\ V^{-1}\ s^{-1}$. It is regarded as one of the excellent inorganic HTMs for dye-sensitized and FE-based PV devices [29–32].

Figures 2(c) and (d) present the microstructures of KBNNO1 planar- and mesostructured solar cells. The cross-sectional SEM image for the NiO/KBNNO1/c-TiO_2/FTO solar cell obviously displays sequential superposition layers of FTO (~360 nm), c-TiO_2 (~40 nm), KBNNO1 (~290 nm), and NiO (~60 nm). This result could also be discussed using a typical line scans of energy dispersive x-ray spectroscopy (EDS), as shown in figure 2(e). It is clear that the profiles of Au Lα, Ni Kα, K Kα Ba Mα, Ti Kα, and Sn Lα were chiseled at the boundaries of contiguous layers. For mesostructured device, the EDS spectra is shown in figure S2(a), in which each elementary peaks can be easily identified. Moreover, laminar morphology and homogeneous elemental distribution from the EDS mapping (figure S2(b)) can be observed. From figure 2(d), the mesoporous layer with a thickness of ≈1.9 μm was observed on top of the planar c-TiO_2 film. It is apparent that the profiles of Au Lα, K Kα Ba Mα, Ti Kα, and Sn Lα in mesostructured solar cell is similar to planar junction (figure 2(f)). However, for mesostructured junction, the profiles of the Ni Kα have no obvious boundaries between different layers, suggesting KBNNO1 and NiO grains can uniformly infiltrate into the pores of m-TiO_2 layer.

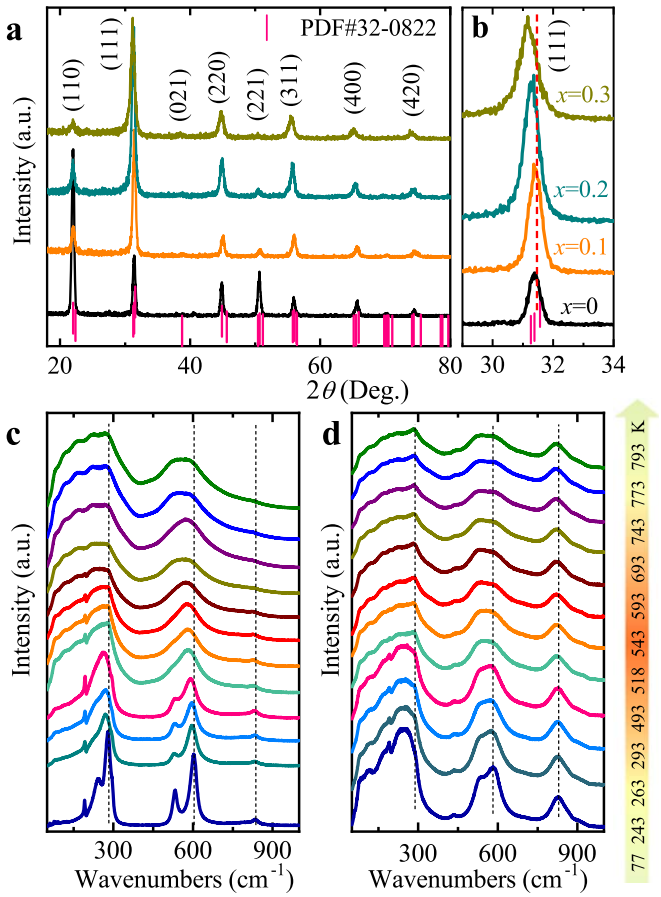

Figure 3. (a) Room-temperature XRD data and (b) enlarged patterns of the KBNNOx films. Raman scattering spectra of (c) KNO and (d) KBNNO1 films at selected temperature. Phase transitions become more obvious in KNO films. Both films exhibit a continuous phase transition of R → O → T → C.

To demonstrate the crystalline quality of the light-absorbing layers, the crystalline structures of the four kinds of as-fabricated films (KNO-KBNNO3) were characterized by XRD, as shown in figure 3(a). Typical single peaks are observed for the end member KNO and doped KBNNOx films. A closer inspection of the shoulders suggests the doped KBNNOx samples belong to an average orthorhombic crystal symmetry. It is clear that the XRD reflections shift toward lower 2θ angles with increasing x, suggesting an increase in the unit cell volume (figure 3(b)). To further illustrate the crystallization, Raman spectra for temperature range of $77\ \mathrm{K} < T < 793\ \mathrm{K}$ were measured for end number KNO and doped KBNNO1 films in the figures 3(c), (d) and S3. Additional stoichiometries could be available in figures S4 and S5. Figures 3(c) and (d) show that a red-shift trend of phonon center positions are obtained caused by lattice thermal expansion. Moreover, KNO and KBNNO1 films are polycrystalline, and the observed signal from Raman spectra is also an average of many oblique angles, which is not strictly associated with phonon wave vectors (neither parallel nor perpendicular to the specific crystallographic axes) [33–35]. Furthermore, according to the group theoretical analysis, the Raman spectrum is mainly identified as (i) a Fano-type interference dip at around ~190 cm^{-1} due to $E(\mathrm{TO}_2, \mathrm{LO}_2) + A_1(\mathrm{TO}_2,\mathrm{LO}_2)$; (ii) a broad $E(\mathrm{TO}_1)$ mode zone centered at 240 cm^{-1}; (iii) a sharp $A_1(\mathrm{TO}_1)$ mode centered at 279 cm^{-1}; (iv) another sharp mode $(E + B_1)(\mathrm{TO}_4,\mathrm{LO}_4)$ at 293 cm^{-1}; (v) a $E(\mathrm{TO}_3)$ at 530 cm^{-1}; (vi) a $A_1(\mathrm{TO}_3)$ at 600 cm^{-1}; (vii) a mixed low intensity $A_1(\mathrm{LO}_3)$ at 830 cm^{-1}. By contrast, the peaks in the KBNNO1 film are much broader, and a peak at ~430 cm^{-1} becomes clearer. Moreover, an obvious characteristic for KBNNO1 sample is that the mode at 830 cm^{-1} was still clearly visible at high temperature, which indicates the presence of a new mode due to the breathing of the octahedra when the B sites were occupied by different cations of Ni^{2+} and Nb^{5+}. From figures 3(c) and (d), we can observe the successive phase transitions from rhombohedral (R, $R3m$) → orthorhombic (O, $Amm2$) → tetragonal (T, $P4mm$) → cubic (C, $Pm\bar{3}m$), which are corresponding to the transition temperature $T_{R\to O} \approx 263$ K, $T_{O\to T} \approx 493$ K, and $T_{T\to C} \approx 693$ K for KNO film, and corresponding to the transition temperature $T_{R\to O} \approx 293$ K, $T_{O\to T} \approx 493$ K, and $T_{T\to C} \approx 743$ K for KBNNO1 film, respectively. Note that all above Raman features except for the relative intensities of KNO and KBNNO1 thin films are fully consistent with the characteristics of KNO and KBNNO1 ceramics, [3, 36] which can be confirmed on the successful preparation of KNO and KBNNO1 thin films.

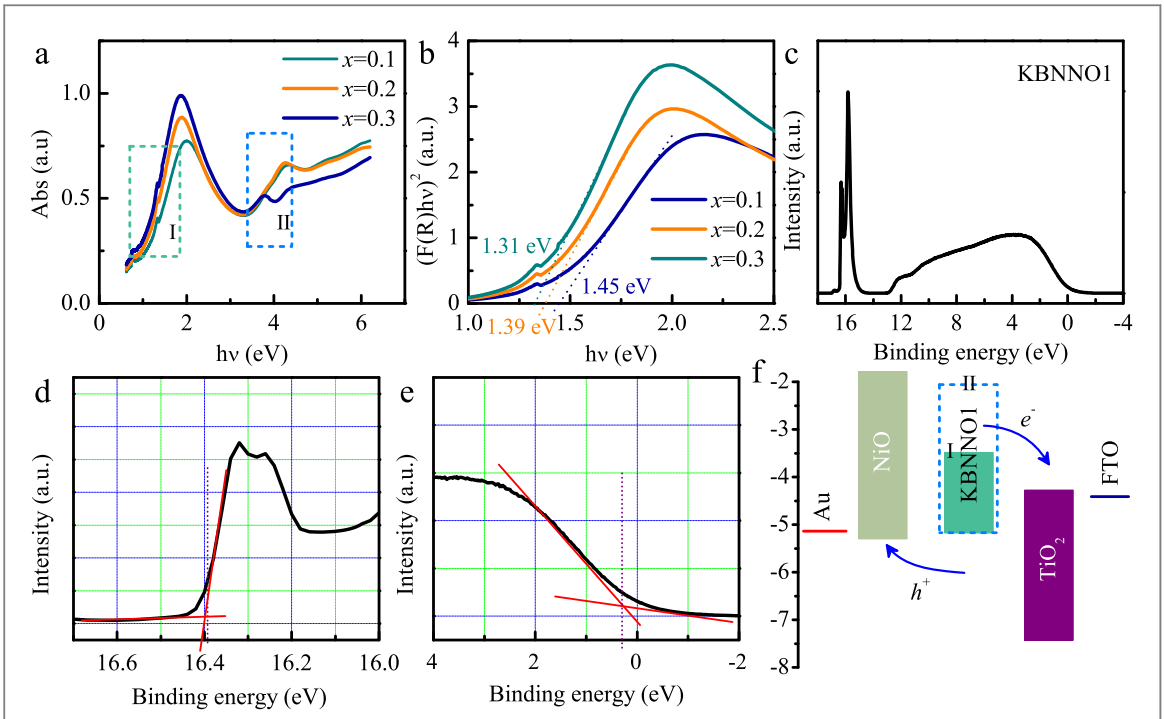

Figure 4. (a) Absorption spectra of the KBNNOx (x = 0.1–0.3) films. (b) Tauc plot of $(\alpha h\nu)^2$ versus $h\nu$ for bandgap determination. For all the samples, the narrow bandgaps are marked by the dotted line, which can be attributed to the defect-related absorbtion caused by V_O. (c) UPS spectrum of KBNNO1 films. (d) UPS secondary cutoff region and (e) UPS valence band region. (f) Energy levels diagram for each components from the PV device.

3.3. Bandgap and energy levels

Figure 4(a) shows the UV–vis-NIR absorption spectra of the KBNNO1, KBNNO2, and KBNNO3 films. It is found that all the samples exhibit double absorbance peaks, as remarked by I and II, indicating that these films have both UV–vis and NIR absorption, as compared with previous reported FE absorbers including the wide-acceptably FE active layers $BiFeO_3$, Bi_2FeCrO_6, and $Pb(Zr,Ti)O_3$ [17, 18, 37–39]. The obvious NIR absorption is attributed to oxygen vacancies (V_O) derived from the Ni^{2+} doping in perovskite B site, which is similar with $Pb(Ti_{1-x}Ni_x)O_{3-x}$ solid solutions [40, 41]. The theoretical results show that there are two stable configurations for the V_O in KBNNOx, Ni^{2+}–V_O–Nb^{5+} and Ni^{2+}–V_O–Ni^{2+}. Thus, it indicates that the combination of metal-oxygen bond results in the lower bandgaps owing to the introduction of the Ni 3d. Whereas, an extra density of states peak, contributed by the d-orbitals of the six-fold-coordinated Ni, is observed in the valence band maximum from Ni^{2+}–V_O–Nb^{5+} [2]. Therefore, the E_g value of the Ni^{2+}–V_O–Nb^{5+} configuration is lower than that of Ni^{2+}–V_O–Ni^{2+} configuration, which can correspond to the new absorbance I and II, respectively. It is noteworthy that the above films have a high concentration of V_O to form recombination centers due to K^+ loss during the sintering process, which hinder the motion of the electron/hole. Therefore, it is necessary to reduce the amount of V_O while preserving the beneficial effects of V_O in reducing the bandgap and enhancing the visible-light absorption [1]. Here, we demonstrate that the hydrolysis at 0 °C of KBNNOx solutions by the addition of the growth medium deionized water could effectively control the concentration for V_O, as well as form the Ni^{2+}–V_O–Nb^{5+} and Ni^{2+}–V_O–Ni^{2+} configurations.

The bandgaps of all doped KBNNOx films can be evaluated utilizing the Tauc plots, as shown in figure 4(b). A new shoulder (I) appears in all doped films. The corresponding bandgaps were extracted from the intercept of the tangent line in the plot of $[F(R)h\nu]^2$ versus energy. It is shown that the direct bandgap is 1.45 eV for x = 0.1, 1.39 eV for x = 0.2, and 1.31 eV x = 0.3, respectively, which agrees with the result of first principle calculation for direct bandgap of 1.49 eV. Moreover, these values are much less than 3.8 eV of the intrinsic bandgap for the KNO. Owing to the bandgap value of 1.45 eV matching well with that of solar spectral center, the KBNNO1 films can be tried for use in FE photovoltaic devices.

Figures 4(c)–(e) depict the onset (E_i) and cutoff ($E_{cut-off}$) energy regions for KBNNO1 film. The E_i and $E_{cut-off}$ energy are 0.28 eV and 16.4 eV, respectively. Its work function (ϕ) can be calculated to be 5.1 eV by the equation $\phi = 21.22 - (E_{cut-off} - E_i)$. Additionally, based on the bandgap values of KBNNO1, energy level diagram of the system components relative to vacuum was constructed. The electron affinities and work functions of carrier transporting-layer and electrode are obtained from the previous reports [29, 31, 42, 43].

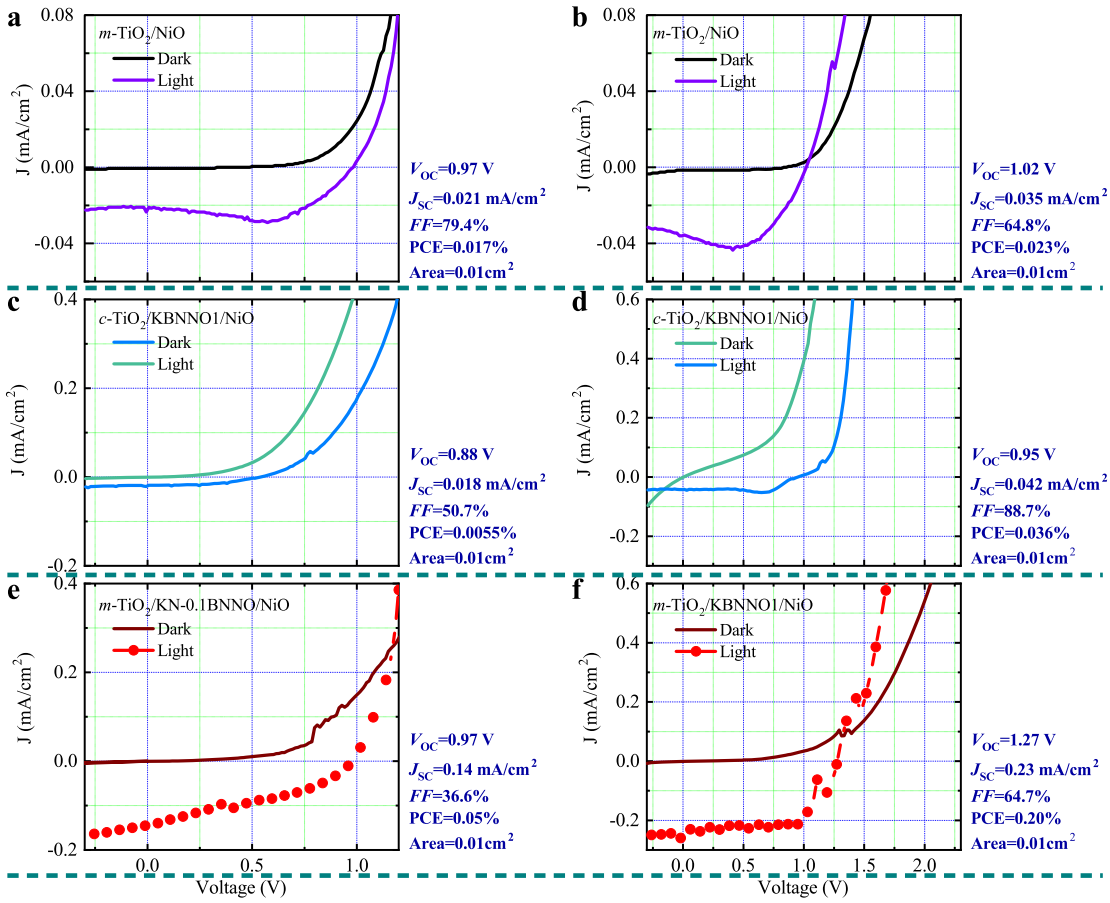

Figure 5. Dark and illuminated *J–V* characteristics of (a), (b) *m*-TiO_2/NiO mesostructured device without KBNNO1 layers, (c), (d) *c*-TiO_2/KBNNO1/NiO planar heterojunction and (e), (f) *m*-TiO_2/KBNNO1/NiO mesostructured heterojunction solar cell at scan from +1.2 to −0.3 V and +2 to −0.3 V, respectively. The J_{SC}, V_{OC}, FF, and PCE of these devices are also given.

As shown in figure 4(f), the band edge positions of the KBNNO1, TiO_2 and NiO are well aligned, which is beneficial for the separation of *e–h* pairs.

3.4. PV performance and analysis

In figures 5(a)–(f), PV performances of the *m*-TiO_2/NiO, *c*-TiO_2/KBNNO1/NiO and *m*-TiO_2/KBNNO1/NiO junctions are characterized and compared. The dark *J–V* curves recorded on three junctions show a low current-density. Under simulated AM 1.5 irradiation, the quasi-linear *J–V* curves for *m*-TiO_2/NiO and *c*-TiO_2/KBNNO1/NiO heterojunctions show a lower PV effect than that of *m*-TiO_2/KBNNO1/NiO device. That is to say, the contribution of the *m*-TiO_2 and NiO layers can be negligible. For the planar-structured *c*-TiO_2/KBNNO1/NiO heterojunction, the *e–h* pairs in the KBNNO1/TiO_2 and KBNNO1/NiO interface regions can be separated and transported to the two terminal electrodes. In contrast, in the mesostructured *m*-TiO_2/KBNNO1/NiO heterojunctions, the generated *e–h* pairs in the KBNNO1 grains can be quickly injected into the *m*-TiO_2 and NiO, resulting in the collection by the electrodes. Figures 5(e) and (f) show the *J–V* curve characterized on the best-optimizing *m*-TiO_2/KBNNO1/NiO solar cell at the voltage scan pulse of 1.2 V and 2 V, respectively. The curves under illumination show the short-circuit current density (J_{SC}) of 0.14 mA cm^{-2}, open-circuit voltage (V_{OC}) of 0.97 V, PCE of 0.05%, and FF of 36% (figure 5(e)), respectively. It illustrates that the PV output increases with increasing the scan bias, which can be extracted from the data of figure 5(f) that $J_{SC} \approx 0.23$ mA cm^{-2}, $V_{OC} \approx 1.27$ V, PCE ≈ 0.2%, and FF ≈ 64%, respectively. The reason for such a increased PV output can be attributed to enhanced light absorption and a possible reduction of the photocharge recombination rate caused by the migration of V_O and polarization flipping. As shown in figure S6(a), the polarization–electric field (*P–E*) loop of the KBNNO1 mesoporous-type solar cell exhibits a linear behavior over the voltage range of −1 to 1 V, which means that no polarization flipping occurs. Figure S6(a) also shows that the polarization flipping can be triggered in KBNNO1 films with increasing the voltage. These results are consistent with the above PV output. It demonstrates that the present *P–E* results are solid evidences to reflect the impaction of PV output induced by the polarization flipping. The detailed physical mechanisms will be discussed in the following.

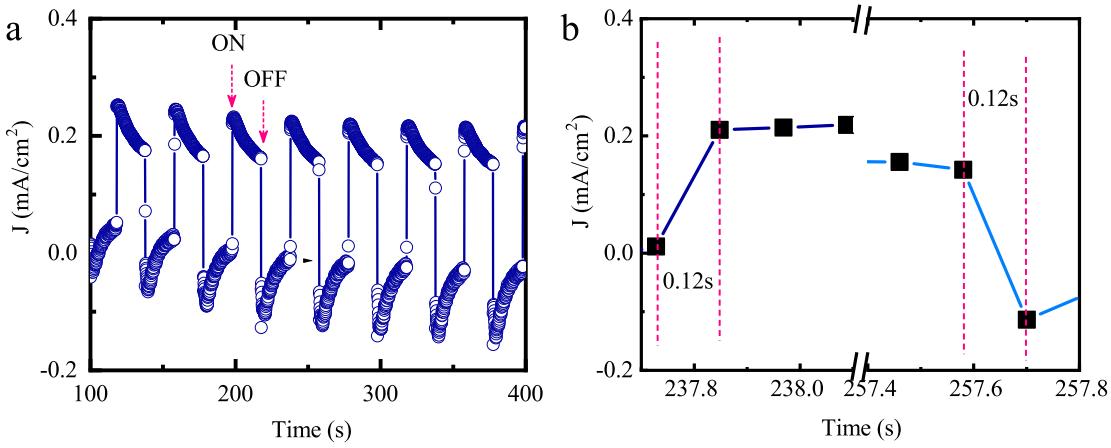

Figure 6. (a) Photoswithing characteristics for the mesostructured heterojunction. (b) Temporal voltage response of mesostructured heterojunction with a rise time of 0.12 s and a decay time of 0.12 s.

Figure 6(a) shows the ON/OFF switching behavior of *m*-TiO_2/KBNNO1/NiO heterojunction under the short-circuit condition. It has been revealed that the photocurrent is consistent and repeatable. The stability of the photoswitching behavior is related to the ferroelectric polarization stability of KBNNO1 layers and the reliability of the *e*–*h* transmission channel. It is worth emphasizing that the V_O plays a significant role in the obtained PV effect. Because of KBNNO1 ferroelectrics with low V_O concentration of 2.5%, the unstable domain state can be suppressed by polarization. Thus, the magnitude of depolarization field shows little change and high stability of the photocurrent over multiple cycles can be observed [22, 44]. On the contrary, for those ferroelectrics with a higher V_O concentration, the domain state after removing the poling field is unstable, where the hopping electrons will recombine with the V_O [44]. Thus, it leads to the monotonous decrease in the magnitude of the photocurrent under the illumination. Here, a decay of photocurrent was also observed. Therefore, it is necessary to control the amount of V_O to ensure the stability and enhanced photocurrent output. Furthermore, the rise and decay times can be deduced to be about 0.12 and 0.12 s from figure 6(b), respectively, which exhibit little temporal change of photocurrent. In our case, the high-sensitivity photoresponse may result from the interface (e.g. TiO_2/KBNNO1 and NiO/KBNNO1) of the mesostructured carrier transporters in PV device. It is clear that the *e*–*h* pairs could be much easier to transport and collect at the interface regions due to the ETM and HTM layers are closely coupled in the mesostructured devices [45]. Those studies on high-sensitivity photoresponse and fast *e*–*h* separation for photovoltaic device with KBNNO1 absorber may find new materials for future applications in perovskite-based photodetector.

3.5. Operation mechanism and hysteretic behavior

For the mesostructured KBNNO1 heterojunctions, the intrinsic build-in fields ($\overrightarrow{E_{bi}}$) generated at the interfaces between FE and carrier transporting-layer, which is the primary driving force for separation of the *e*–*h* pairs. However, switchable polarization and redistribution of V_O [21, 37, 46, 47], could also play an important role in enhancement of the PV effect. To better understand the contributions of above factors, the different scanning voltage range and direction were applied on KBNNO1 solar cells during the photocurrent measurement under illumination. In the measurement process, all applied voltage was on the Au electrode and FTO electrode was always grounded. In order to prevent the breakdown and irreversible reversal of these devices, the maximum positive voltage (V_m) was carefully controlled below 8 V. Forward and reverse scans are recorded as the voltage scanned from $-V_m$ to V_m and V_m to $-V_m$, respectively. The V_m dependent J_{SC}, V_{OC}, and PCE were extracted from the *J*–*V* characteristics under reverse (forward) scan, which can also indicate the *J*–*V* hysteretic behavior, as presented in figures 7(a)–(c), S6(b) and (c). Apparently, the *J*–*V* curves of the reverse scan exhibit a enhance tendency with V_m increasing, and finally reach the saturated state. However, the extracted J_{SC}, V_{OC}, and PCE from the forward-scanned *J*–*V* characteristics are lower than those of the reverse scanning, resulting in lower PV output. Moreover, because of the completely polarization of the KBNNO1 light absorber layer under reverse scan from +8 to −0.3 V, the maximum PCE is measured up to 1%.

The phenomena of the above reverse and forward rectifying signal of the KBNNO1 PV devices can be explained by modulated energy band due to FE polarization and V_O, as reported by Maksymovych *et al* [48]. Electromigration of the V_O and switchable FE polarization can change the width of the depletion regions inside the FE absorber, which could regulate the *J*–*V* curves at different scanning history, as previously discussed [49–51]. To clarify the different interface band and PV effects for KBNNO1 heterojunctions under varied

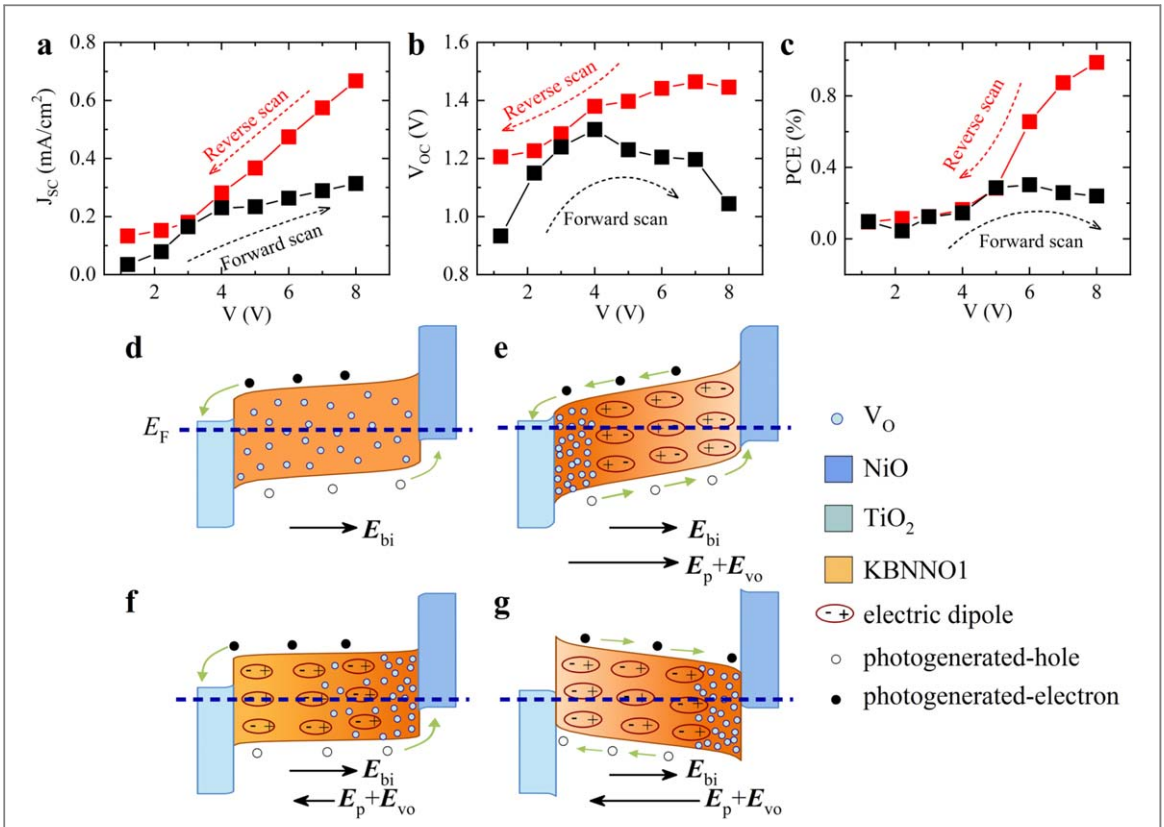

Figure 7. The V_m dependent (a) J_{SC}, (b) V_{OC}, and (c) PCE extracted from the *J–V* characteristics under reverse and forward scan. Schematic of electronic band structure for *m*-TiO_2/KBNNO1/NiO device after various scanning histories. (d) Original, (e) after reverse scan from V_m to 0, (f) after forward scan from $-V_m$ to 0 with small V_m, (g) after forward scan from $-V_m$ to 0 with large V_m. In above diagram, the circles and ellipses represent the V_O and FE polarized domains, respectively. The E_p and E_{VO} represent the additional build-in field caused by polarization and the migration of V_O, respectively. The solid arrows represent the direction of build-in electric fields and the drift directions of electron/hole.

scanning voltage range and direction, the detailed rectification process for photovoltaic properties and electronic band structure for devices at short-circuit condition are described sequentially in figures 7(e)–(g), respectively. As shown in figure 7(e), without applying the electric field, the V_O can be distributed homogeneously inside the polycrystalline KBNNO1 grains. In this case, KBNNO1 films have no self-polarization. The interface band structures of KBNNO1 are regulated only by the two transporting-layers at the interface regions. Grinberg *et al* have demonstrated that the KBNNO1 material is a *n*-type semiconductor because V_O serves as electron donors [1, 52, 53]. Thus, the *p*-*n* and n^+-*n* junctions are formed at the interfaces of NiO/KBNNO1 and TiO_2/KBNNO1. The $\overrightarrow{E_{bi1}}$ and $\overrightarrow{E_{bi2}}$ have the same direction. The total build-in field can be written as $\overrightarrow{E_{bi}} = \overrightarrow{E_{bi1}} + \overrightarrow{E_{bi2}}$, which is the primary force for separation of the photon-generated *e*–*h* pairs.

By controlling the voltage pulses applied on the solar cell, KBNNO1 grains can be polarized. Meanwhile, the charged V_O can move toward the other end of the ferroelectric layer to achieve a new equilibrium state. It has been reported that the high concentration V_O layer in the interface can reduce the barrier height of the *n*-type films, which is similar to an extra build-in field ($\overrightarrow{E_{VO}}$) applied on the heterojunction. In the scanned process, although the applied voltage can be decreased to 0, the remained asymmetric distribution of V_O and $\overrightarrow{P_r}$ could modify the interface band structures of KBNNO1, resulting in varied PV output. Under the reverse scanned from V_m to 0, the positive bias leads to V_O move toward TiO_2/KBNNO1 interface and create $\overrightarrow{P_r}$ pointing toward TiO_2 side. The accumulation of V_O and FE polarization charges induce a heavily doped n^+ layer, which leads to a downward-bending for KBNNO1 energy bands in the TiO_2/KBNNO1 interface region. Meanwhile, the NiO/KBNNO1 interface region is depleted, thus reducing the KBNNO1 energy band at this end [19, 44, 54–57]. To quality the impact of V_O and polarization for PV output, an additional build-field field derived from the combination of V_O and polarization can be defined as $\overrightarrow{E_{VO}} + \overrightarrow{E_P}$, which has the same direction with $\overrightarrow{E_{bi}}$ and enhances the PV effect. Because large reserve scanning voltage will increase $\overrightarrow{P_r}$ and the density of V_O in the TiO_2/KBNNO1 interface region, a monotonic enhancement of PV parameters as V_m increases is obtained.

In contrast, under a forward bias scanned from $-V_m$ to 0, the negative bias on the NiO electrode promotes the accumulating of V_O at the NiO/KBNNO1 interface and generates P_r pointing toward the NiO side. Thus, the $\overrightarrow{E_P} + \overrightarrow{E_{VO}}$ and $\overrightarrow{E_{bi}}$ have opposite directions. For a small voltage pulse V_m (figure 7(f)), $|\overrightarrow{E_P} + \overrightarrow{E_{VO}}| < |\overrightarrow{E_{bi}}|$,

it reduces the net build-in field. As a result, in the NiO/KBNNO1 interface region, a recombination between the photon-generated holes and the V_O-trapped electrons will be generated before collecting by the NiO. Additionally, the recombination rate decreases with increasing scanning voltage, until the scanning voltage is close to the breakdown voltage. Furthermore, when V_m is large enough to make $|\overrightarrow{E_P} + \overrightarrow{E_{VO}}| > |\overrightarrow{E_{bi}}|$, the inverted net build-in field makes e toward the NiO side and h toward the TiO_2 side. That is to say, NiO and TiO_2 layers become the energy barriers, only the photocarriers with higher energy can overcome this barrier hight and be collected by electrodes (figure 7(g)). In conclusion, even though the forward scanning with large V_m can improve the PV output, the J_{SC} and V_{OC} are less than those of observed in the reverse scanning. The above mechanisms have provided deep insights into how V_O and polarization affect the PV effect in KBNNO1 solar cells.

4. Conclusions

It is noteworthy that the strategy reported here is summarized from the novel single-phase $(KNbO_3)_{1-x}(BaNi_{1/2}Nb_{1/2}O_{3-\delta})_x$ ($x = 0, 0.1, 0.2$, and 0.3) films as a technological breakthrough for the preparation of $KNbO_3$-based films. Furthermore, the bandgap tunability has been firstly established by applying growth medium (deionized water) as the reaction nucleation sites in KBNNOx films. It is found that the bandgaps of the new films can be substantially reduced to 1.45 eV, matching well with the solar spectral center (~1.5 eV). Subsequently, we successfully combine the mesostructured electron-transporting TiO_2 and hole-transporting p-type NiO layers with perovskite KBNNO1 in dye-sensitized PV device. Such structural device takes advantage of the large area of light-absorption layer and good ferroelectric properties of KBNNO1 in photoelectric conversion devices, which can contribute to a high PV output for $KNbO_3$-based solar cells. Moreover, the intrinsic FE polarization and oxygen vacancies electromigration in KBNNO1 can also be beneficial to the transformation from Schottky-like barrier to Ohmic contacts, thus tailoring the PV performance. Therefore, the present work opens a new avenue to discover and design optimal ferroelectric film based solar cells with improved efficiency. Finally, the high-sensitivity photoresponse and fast e–h separation for photovoltaic device with KBNNO1 absorber layers will open up new materials for future developments of novel generation perovskite-based photodetector.

Acknowledgments

This work was financially supported by the National Key R&D Program of China (Grant Nos. 2017YFA0303403 and 2018YFB0406500), the National Natural Science Foundation of China (Grant Nos. 61674057 and 61227902), the Projects of Science and Technology Commission of Shanghai Municipality (Grant Nos. 18JC1412400, 18YF1407200, and 18YF1407000), and the Program for Professor of Special Appointment (Eastern Scholar) at Shanghai Institutions of Higher Learning and the Fundamental Research Funds for the Central Universities.

ORCID iDs

Zhigao Hu https://orcid.org/0000-0003-0575-2191

References

[1] Grinberg I *et al* 2013 *Nature* **503** 509
[2] Wang F G and Rappe A M 2015 *Phys. Rev.* B **91** 165124
[3] Li C Q, Wang F, Sun Y S, Jiang K, Gong S J, Hu Z G, Zhou Z Y, Dong X L and Chu J H 2018 *Phys. Rev.* B **97** 094109
[4] Glass A M, Von der Linde D and Negran T J 1974 *Appl. Phys. Lett.* **25** 233
[5] Josch W, Munser R, Ruppel W and Wurfel P 1978 *Ferroelectrics* **21** 623
[6] Koch W T H, Munser R, Ruppel W and Wurfel P 1975 *Solid State Commun.* **17** 847
[7] Han H, Song S, Lee J H, Kim K J, Kim G-W, Park T and Jang H M 2015 *Chem. Mater.* **27** 7425
[8] Yang S Y *et al* 2010 *Nat. Nanotechnol.* **5** 143
[9] Alexe M and Hesse D 2011 *Nat. Commun.* **2** 256
[10] Chanussot G 1978 *Ferroelectrics* **20** 37
[11] Kreisel J, Alexe M and Thomas P A 2012 *Nat. Mater.* **11** 260
[12] Young S M and Rappe A M 2012 *Phys. Rev. Lett.* **109** 116601
[13] Choi W S, Chisholm M F, Singh D J, Choi T, Jellison G E Jr and Lee H N 2012 *Nat. Commun.* **3** 689
[14] Qin M, Yao K and Liang Y C 2008 *Appl. Phys. Lett.* **93** 122904
[15] Bhatnagar A, Chaudhuri A R, Kim Y H, Hesse D and Alexe M 2013 *Nat. Commun.* **4** 2835
[16] Lee W M, Sung J H, Chu K, Moya X, Lee D, Kim C J, Mathur N D, Cheong S W, Yang C H and Jo M H 2012 *Adv. Mater.* **24** OP49

[17] Luisman L, Feteira A and Reichmann K 2011 *Appl. Phys. Lett.* **99** 192901
[18] Nechache R, Harnagea C, Li S, Cardenas L, Huang W, Chakrabartty J and Rosei F 2014 *Nat. Photon.* **9** 61
[19] Fang L, You L, Zhou Y, Ren P, Lim Z S and Wang J L 2014 *Appl. Phys. Lett.* **104** 142903
[20] Zhang G H, Wu H, Li G B, Huang Q Z, Yang C Y, Huang F Q, Liao F H and Hua J H 2013 *Sci. Rep.* **3** 1265
[21] Ji W, Yao K and Liang Y C 2010 *Adv. Mater.* **22** 1763
[22] Song B Q *et al* 2017 *J. Alloy. Compd.* **703** 67
[23] Wang K and Li J F 2010 *Adv. Funct. Mater.* **20** 1924
[24] Wang K, Yao F Z, Jo W, Gobeljic D, Shvartsman V V, Lupascu D C, Li J F and Rödel J 2013 *Adv. Funct. Mater.* **23** 4079
[25] Wang X P, Wu J G, Xiao D Q, Zhu J G, Cheng X J, Zheng T B, Zhang Y, Lou X J and Wang X J 2014 *J. Am. Chem. Soc.* **136** 2905
[26] Wang X P, Wu J G, Xiao D Q, Cheng X J, Zheng T B, Zhang Y, Lou X J and Zhu J G 2014 *J. Mater. Chem.* A **2** 4122
[27] Grätzel M 2003 *J. Photovhem. Photobiol.* C **4** 145
[28] Hagfeldt A, Boschloo G, Sun L, Kloo L and Pettersson H 2010 *Chem. Rev.* **110** 6595
[29] Irwin M D, Buchholz D B, Hains A W, Chang R P H and Marks T J 2008 *Proc. Natl Acad. Sci.* **105** 2783
[30] Bandara J and Weerasinghe H 2005 *Sol. Energy Mater. Sol. Cells* **85** 385
[31] Jeng J Y, Chen K C, Chiang T Y, Lin P Y, Tsai T D, Chang Y C, Guo T F, Chen P, Wen T C and Hsu Y J 2014 *Adv. Mater.* **26** 4107
[32] Wang L F *et al* 2015 *Phys. Rev. Appl.* **3** 064015
[33] Loudon R 1964 *Adv. Phys.* **13** 423
[34] Postnikov A V and Borstel G 1994 *Phys. Rev.* B **50** 16403
[35] Pruzan P H, Gourdain D and Chervin J C 2007 *Phase Transit.* **80** 1103
[36] Hawley C J, Wu L Y, Xiao G, Grinberg I, Rappe A M, Davies P K and Spanier J E 2017 *Phys. Rev.* B **96** 054117
[37] Choi T, Lee S, Choi Y J, Kiryukhin V and Cheong S-W 2009 *Science* **324** 63
[38] Zheng F G *et al* 2014 *J. Mater. Chem.* A **2** 1363
[39] Wang D, Yuan G L, Hao G Q and Wang Y J 2018 *Nano Energy* **43** 351
[40] Gou G Y, Bennett J W, Takenaka H and Rappe A M 2011 *Phys. Rev.* B **83** 205115
[41] Kondo M and Kurihara K 2001 *J. Am. Ceram. Soc.* **84** 2469
[42] Chung I, Lee B, He J Q, Chang R P H and Kanatzidis M G 2012 *Nature* **485** 486
[43] Fan Z, Yao K and Wang J 2014 *Appl. Phys. Lett.* **105** 162903
[44] Guo Y P, Guo B, Dong W, Li H and Liu H Z 2013 *Nanotechnology* **24** 275201
[45] Bera A, Wu K W, Sheikh A, Alarousu E, Mohammed O F and Wu T 2014 *J. Phys. Chem.* C **118** 28494
[46] Yi H T, Choi T, Choi S G, Oh Y S and Cheong S W 2011 *Adv. Mater.* **23** 3403
[47] Ji W, Yao K and Liang Y C 2011 *Phys. Rev.* B **84** 094115
[48] Maksymovych P, Jesse S, Yu P, Ramesh R, Baddorf A P and Kalinin S V 2009 *Science* **324** 1421
[49] Yang C-H *et al* 2009 *Nat. Mater.* **8** 485
[50] Yin K B, Li M, Liu Y W, He C L, Zhuge F, Chen B, Lu W, Pan X Q and Li R-W 2010 *Appl. Phys. Lett.* **97** 042101
[51] Wang C, Jin K-J, Xu Z-T, Wang L, Ge C, Lu H-B, Guo H Z, He M and Yang G-Z 2011 *Appl. Phys. Lett.* **98** 192901
[52] Mogilevsky R, Levi-Setti R, Pashmakov B, Liu L, Zhang K, Jaeger H M, Buchholz D B, Chang R P H and Veal B W 1994 *Phys. Rev.* B **49** 6420
[53] Janousch M, Meijer G I, Staub U, Delley B, Karg S F and Andreasson B P 2007 *Adv. Mater.* **19** 2232
[54] Wang Y, Jiang Q-H, He H C and Nan C-W 2006 *Appl. Phys. Lett.* **88** 142503
[55] Moubah R, Rousseau O, Colson D, Artemenko A, Maglione M and Viret M 2012 *Adv. Funct. Mater.* **22** 4814
[56] Zhou Y, Fang L, You L, Ren P, Wang L and Wang J L 2014 *Appl. Phys. Lett.* **105** 252903
[57] Yuan G L and Wang J L 2009 *Appl. Phys. Lett.* **95** 252904